Several Orders of Magnitude Difference in Charge Transfer Kinetics Induced by Localized Trapped Charges on Mixed Halide Perovskites

*Izuru Karimata,[†] Kaoru Ohta,[†,‡] Yasuhiro Kobori,[†,‡] and Takashi Tachikawa[†,‡,]**

[†] Department of Chemistry, Graduate School of Science, Kobe University, 1–1 Rokkodai–cho, Nada–ku, Kobe 657–8501, Japan

[‡] Molecular Photoscience Research Center, Kobe University, 1–1 Rokkodai–cho, Nada–ku, Kobe 657–8501, Japan

KEYWORDS. partial halide substitution, photoluminescence microscopy, charge transfer, space charge region, diffusion model

ABSTRACT

Partial halide substitution in organolead halide perovskites $MAPbX_3$ ($MA = CH_3NH_3^+$, $X = Cl^-$, Br^-, or I^-) leads to semiconductor heterostructures with precisely tuned band-gap energies, which facilitates efficient charge extraction or separation for high-performance solar cells and optoelectronic devices. In this study, partially iodide-substituted $MAPbBr_3$ perovskites were prepared through a halide-exchange reaction in the liquid phase, and in-situ space and time-resolved photoluminescence (PL) profiles were acquired by means of confocal microscopy. The rates of charge transfer from the bulk $MAPbBr_3$ to the surface $MAPbBr_{3-x}I_x$ domains, which are widely distributed over a single crystal, were found to greatly depend on the excitation power density. In particular, an abnormally slow charge-transfer process, lasting a few nanoseconds, was observed at higher excitation density. To explain the dependence of this rate on the excitation density, and its correlation with the charge-trapping rate in the bulk $MAPbBr_3$, we propose a plausible mechanism in which trap filling associated with surface-trapped holes induces band bending within the space charge region. This band bending modulates carrier dynamics near the surface, thereby leading to efficient charge extraction from the bulk. In order to validate the mechanism, the carrier dynamics was numerically simulated using a diffusion model that includes the effect of the localized electric field. Our findings provide significantly deeper insight into the carrier dynamics within heterostructured perovskites with nanoscale heterogeneities, and a robust route for manipulating the photogenerated charges in various types of perovskite devices.

INTRODUCTION

Organolead halide perovskites $MAPbX_3$ ($MA = CH_3NH_3^+$, $X = Cl^-$, Br^-, or I^-) possess excellent photophysical properties, such as high optical absorption coefficients, low exciton binding energies, and long charge-carrier diffusion lengths.[1–3] These prominent features enable these materials to establish high-efficiency photovoltaic cells with conversion efficiencies up to 22.7%.[4] In addition, perovskites exhibit excellent optoelectronic properties that have found applications in light emitting diodes (LEDs) and lasers.[5,6]

To realize these perovskite devices, much effort has been devoted to adapting a number of chemical-composition methods, including Lewis-base treatment,[7,8] cationic ($CH_3NH_3^+$ and $HC(NH_2)_2^+$)) methods, and halide engineering,[9,10] among others. The addition of a Lewis base (e.g., pyridine) into a $MAPbI_3$ film was found to passivate surface defects and positively affect device performance.[7,8] Jeon et al. reported that the incorporation of $MAPbBr_3$ into $FAPbI_3$ ($FA = HC(NH_2)_2^+$) improves the stability of the $FAPbI_3$ phase and increases efficiency.[9] Mixed-halide perovskite precursors also lead to enhanced stabilities and carrier features of the resulting perovskites.[10,11] As another approach, Kim et al. developed a method for partial halide substitution that improves the stabilities and efficiencies of perovskite solar cells.[12] By introducing bromide ions into the $MAPbI_3$ film with an HBr solution, the halide concentration gradient was demonstrated to provide efficient carrier extraction, a consequence of precise band-gap tuning. Moreover, Tian et al. demonstrated enhanced long-distance carrier transport in bromide-gradient $MAPbBr_{3-x}I_x$ single-crystalline nanowires that were synthesized by a solid-to-solid halide-exchange reaction.[13] In this way, partial halide substitution involving a halide-exchange reaction, which provides heterostructured perovskite crystals in which the intrinsic carrier features are significantly altered during the synthesis procedure, has become a promising strategy for the

preparation of more efficient perovskite devices. Developing a fundamental understanding of the structure-related carrier dynamics is therefore essential for well-controlled exchange reactions and efficient carrier extraction from perovskite films. However, the underlying mechanism related to the excitation power dependence and nanosized surface domains remains unclear because nanoscopic heterogeneities inherent in the structures and reaction dynamics are difficult to resolve by conventional bulk-measurement techniques.

In this work, mixed halide perovskite crystals with iodide concentration gradients ($MAPbBr_{3-x}I_x$) were prepared in order to investigate the carrier dynamics in these heterostructures. Our previous study revealed that dynamic halide-exchange reactions produce nanometer-scale iodide-rich domains on individual $MAPbBr_3$ crystals, and such surface domains effectively collect photogenerated charges from the bulk $MAPbBr_3$.[14] At the same time, we specifically questioned how such heterostructures affect the carrier dynamics in the whole crystal. Considering that carrier dynamics are affected by the local compositions of halide ions, further investigations into carrier dynamics at the nanoscale level are required in order to unravel the relationship between them. Herein, we performed space- and time-resolved photoluminescence (PL) experiments using confocal microscopy, and eventually discovered a counterintuitive kinetic trend in which the radiative charge-recombination rates *decrease* with increasing concentration of photogenerated carriers. More specifically, a significantly slow charge-transfer process, over a few dozen nanoseconds, was observed within the heterostructure at higher excitation intensities. We propose a plausible mechanism in which band bending caused by $MAPbBr_3$-surface-trapped holes is responsible for controlling the charge-transfer process. To validate this mechanism, the temporal evolution of PL was numerically simulated using a diffusion model that included a localized electric field.

RESULTS AND DISCUSSION

We synthesized microsized $MAPbBr_3$ crystals by following the method previously reported by us (see Experimental Section for synthesis procedures).[14] Figure 1A shows an optical image of an $MAPbBr_3$ crystal spin-coated on a glass coverslip. To investigate the charge-carrier dynamics in individual $MAPbBr_3$ crystals during the halide exchange reaction, in-situ PL measurements were performed using a home-built confocal fluorescence microscope. $MAPbBr_3$ crystals were excited by diffraction-limited picosecond pulses from a 405-nm diode laser, which is visualized as a bright green PL spot in Figure 1B.

The exchange reaction in the liquid phase (heptane) was initiated (at $T = 0$ s) by the addition of 20 μL of a reaction solution of MAI ([MAI] = 0.22 mM in a 20:1 v/v mixture of heptane and 2-propanol).[14] As previously reported,[14] the 540-nm peak rapidly decreased after the addition of MAI, and subsequently a new PL peak appeared at 644 nm, gaining intensity over time and eventually red-shifting to ca. 700 nm. Figure 1C displays the PL decay curves observed for a single $MAPbBr_3$ crystal during the course of the reaction. Before reaction (black line), the PL decay curve as a function of the delay time (t) after the light pulse was well fitted by a biexponential decay function with a mean (intensity-weighted) lifetime ($\langle\tau\rangle$) of 2.3 ns (the fast (τ_1) and slow (τ_2) components were 2.2 ns and 18.3 ns, respectively). The mean lifetime is comparable to those reported for microsized perovskite crystals (~2 ns),[5,15] indicating that our sample was highly crystalline. The τ_1 and τ_2 components are attributed to charge trapping by defects and radiative recombination, respectively.[16] However, immediately after the onset of the reaction, much faster PL decay was observed ($\langle\tau\rangle$ = 0.31 ns after 4 s and $\langle\tau\rangle$ = 0.32 ns after 8 s). This rapid PL quenching was

observed in our previous study[14] and is attributed to two reaction processes. Firstly, for the $MAPbBr_3$ crystals partly substituted with a small amount of iodide ions ($0 < x < 1$ in $MAPbBr_{3-x}I_x$), the energy difference between the conduction-band (CB) levels of $MAPbBr_3$ in the bulk core and $MAPbBr_{3-x}I_x$ on the surface is comparable to thermal energy at room temperature (~0.025 eV), while the difference in the valence-band (VB) energies is deep enough to capture holes in the I-rich domains.[12,17] These band structures result in free (mobile) electrons that are delocalized between $MAPbBr_3$ and $MAPbBr_{3-x}I_x$ and (immobile) holes localized at $MAPbBr_{3-x}I_x$, which suppresses radiative recombination. Secondly, with the oxidation potential of I^- (+1.2–1.3 V vs. normal hydrogen electrode (NHE))[18] in mind, the photogenerated holes in the pure $MAPbBr_3$ phase (+1.9 V vs. NHE) are effectively captured by iodide ions adsorbed at the surface, resulting in PL quenching. It is noteworthy that our previous study has shown that neither the crystalline structure changes nor the morphological degradation were detectable during the reaction from the X-ray diffraction (XRD) and scanning electron microscope (SEM) measurements.[14]

Interestingly, the PL decay profile exhibited a rise component at $T \geq 16$ s after adding the MAI solution. Also, the rise contribution increased with increasing reaction time T. This component clearly indicates the formation of $MAPbBr_{3-x}I_x$, which enables charge extraction from $MAPbBr_3$ and resulting in PL from the $MAPbBr_{3-x}I_x$ domain. X-ray photoelectron spectroscopy (XPS) revealed the absence of iodide on the crystal surface after 1-min of reaction time, which is ascribable to the very low concentration of MAI, whereas analyses of crystals treated with a more-concentrated MAI solution for 1 h revealed that iodide ions had penetrated to a depth of ~25 nm from the surface.[14] These results indicate that, during the initial stage of the reaction, $MAPbBr_{3-x}I_x$ exists only on the surface of the $MAPbBr_3$ crystal as a thin layer or as isolated domains with sizes of a few nanometers or less. Considering that the light-penetration depth is ~120 nm ($= 1/\alpha$) , as

determined from the absorption coefficient of $MAPbBr_3$ ($\alpha = 8.5 \times 10^4$ cm^{-1} at 405 nm),[19] the fraction of photogenerated charges near the surface are transferred to the surface $MAPbBr_{3-x}I_x$, resulting in an increase in PL by the radiative electron-hole recombination. The possibility of fluorescence resonance energy transfer (FRET) from $MAPbBr_3$ to $MAPbBr_{3-x}I_x$ is ruled out as discussed below.

The crystals exhibited two PL peaks at $T > 3$ min, at ~540 and ~710 nm, which correspond to $MAPbBr_3$ and $MAPbBr_{3-x}I_x$, respectively; they did not undergo any further change during the course of the experiment (Figure S1). To investigate carrier dynamics, the PL time profiles of the $MAPbBr_3$ and $MAPbBr_{3-x}I_x$ phases were separately acquired at the same location using appropriate bandpass filters (510–560 nm and 663–800 nm, respectively). A rise in the PL of $MAPbBr_{3-x}I_x$ (red trace) is clearly evident in Figure 2A, which is suggestive of charge transfer from the bulk to the surface $MAPbBr_{3-x}I_x$ domains. Each PL profile was nicely fitted to a triexponential function in order to determine decay and rise times. The $MAPbBr_3$ phase exhibits three decay components ($\tau_1 = 0.1$ ns, $\tau_2 = 2.6$ ns, and $\tau_3 = 60$ ns), while the profile for $MAPbBr_{3-x}I_x$ was well reproduced by a single rise component ($\tau_{rise} = 0.45$ ns) and two decay components ($\tau_1 = 3.7$ ns and $\tau_2 = 10$ ns). Importantly, the rise time did not coincide with the decay time of the $MAPbBr_3$ phase. Considering that the PL of $MAPbBr_3$ can be reabsorbed by the $MAPbBr_{3-x}I_x$ domains due to the spectral overlap, fluorescence resonance energy transfer (FRET) would more or less contribute to the PL of $MAPbBr_{3-x}I_x$. The discrepancy between these two kinetics results indicates that the photogenerated electrons and holes in $MAPbBr_3$ migrate independently to $MAPbBr_{3-x}I_x$, which excludes the dominant contribution of FRET to the rise component. Considering that the energy difference in the CB levels of $MAPbBr_3$ and $MAPbBr_{3-x}I_x$ (0.1 eV) is much smaller than that of the VB levels (0.6 eV), interfacial hole transfer should be faster than

electron transfer. Therefore, we suggest that the faster $MAPbBr_3$ decay component (τ_1 = 0.1 ns) corresponds to hole transfer, while the rise component of $MAPbBr_{3-x}I_x$ (τ_{rise} = 0.45 ns) corresponds to electron transfer. The value of this transfer time is within the range previously reported (0.3–0.75 ns) for charge transfer from the $MAPbI_3$ perovskite to the transport layer (TiO_2, PCBM, or spiro-OMeTAD).[20,21] It is however noteworthy that several groups have studied the charge-transfer kinetics from the bromide perovskites to the iodide-rich perovskites (both Cs^+ and MA^+ type) and have reported significantly small values of 0.5–5 ps.[22,23] The present slower transfers can be explained by considering that $MAPbBr_{3-x}I_x$ presents only at the surface as nanosized domains because of the very low amount of MAI added.

Figures 2B and 2C display the excitation-intensity dependences of the PL decay profiles (T > 5 min). Counterintuitively, the rise times for $MAPbBr_{3-x}I_x$ PL were observed to increase with increasing excitation intensity, while the decay profiles for $MAPbBr_3$ PL exhibited little change. In particular, the time constant of the rise component was 32 ns at the higher intensity, indicating that the charge-transfer process takes a few dozen nanoseconds. As mentioned elsewhere,[23,24] intense light induces ion migration in mixed-halide perovskites, leading to phase segregation and subsequent decomposition. During our experiments (T > 3 min), however, the PL profiles and spectra did not change, which excludes such phase segregation and degradation. Moreover, a heat accumulation effect can be excluded as a possible cause because no spectral shift was observed during the measurement of the intensity dependence.[25] One possible reason for the very slow charge transfer process observed here involves the diffusion of charge carriers in the bulk $MAPbBr_3$ followed by charge transfer to the surface $MAPbBr_{3-x}I_x$. Previous studies reported that the diffusion coefficient D of the charge carriers in $MAPbBr_3$ range from 0.1 to 1.44 $cm^2\ s^{-1}$.[26] Adopting the value of the rise time at the higher excitation intensity (τ_{rise} = 32 ns) at the higher

excitation intensity, the diffusion length L_D (= $\sqrt{6D\tau_{rise}}$) in three-dimensional space can be estimated to be 1–5 μm. The rectangular length of an $MAPbBr_3$ crystal ranges from 3 to 10 μm, which allows charge carriers to diffuse almost over the entire crystal. In our experiments, charge carriers are generated near the surface by the focused 405-nm laser, not in the bulk, with PL detected from the same position as the excitation spot by confocal microscopy. Driven by the concentration gradient, the photogenerated carriers diffuse from the surface to the bulk. However, when the diffusion process results in a slow rate of charge transfer, the diffusing carriers inside the crystal must be transferred to the surface against the concentration gradient. Therefore, the contribution of the diffusion process alone cannot account for the unusual charge-transfer process as well as the excitation-intensity dependence of the rise time. Previous reports have revealed that the PL propagates in the perovskite crystals because of the photon recycling leading to the prolonged PL lifetime, in which PL was collected from the area micrometer away from the excitation position.[27,28] In our measurements, the excitation and collection were performed at the same positions; thus it can be considered that photon recycling has little contribution.

To date, the migrations of ions and vacancies have been shown to induce space charge regions at the interfaces between perovskites and transport layers under open-circuit conditions, resulting in *I-V* hystereses, light-soaking, and degradation.[29–31] Moreover, the space charge regions in perovskites result in band bending, which inhibits charge transfer to TiO_2.[32–34] No bias was applied during our experiments, and no p-n junction with TiO_2 was even present. However, it seems plausible that localized charge distributions exist at the surface due to adsorbed or interstitial I^- and MA^+ ions during the halide-exchange reaction involving the MAI solution. The PL decay profiles in Figure 1C clearly reveal that the time integrated intensities and lifetimes following the exchange reaction were lower compared to those before the reaction, which indicates that

structural defects, such as vacancies and interstitial ions, are produced during the reaction and remain at the surface. Photogenerated carriers can be trapped at the defect sites, leading to the formation of a space charge region. Hence, band bending due to ions or trapped carriers is possibly the reason for the observed slow charge-transfer process. The nature of the defect sites will be discussed below.

To clarify the transient species responsible for the observed slow charge transfers, PL decay experiments were performed over different pulse-repetition frequencies (1–10 MHz). Figure 3A displays PL time profiles for the $MAPbBr_{3-x}I_x$ phase; the slow components clearly become more prominent with increasing frequency. The accumulation of ions at the interface between a perovskite and TiO_2 has recently been reported to take from a few microseconds to seconds under both electrical bias and photoirradiation, which induces ion migration due to the space charge region.[29,35,36] However, this time scale for ion accumulation is much longer than the pulse interval ($< 10^{-6}$ s) employed herein. Hence, the origin of band bending is possibly attributable to trapped photocarriers. In $MAPbX_3$ perovskites, the relaxation times of trapped carriers are a few hundred nanoseconds.[16,37,38] The trapped carriers can accumulate at the high excitation intensity or the high pulse-repetition frequency due to the slower relaxation time compared to the charge generation time. The photogenerated-carrier lifetime increases with increasing excitation intensity because the filled trap states can no longer act as traps; this phenomenon is known as the "trap-filling effect".[37,38] Our observations imply that trap filling at the surface leads to localized charge distributions that generate band bending. The trap states should readily be occupied at the higher pulse frequency because the pulse interval is shorter than the relaxation time of the trapped carriers. This interpretation is also supported by the observation that the charge-transfer rate decreases with increasing excitation intensity (Figure 2C). It is likely that trapped carriers remain at the trap sites

for at least 100 ns, when the period of a 10-MHz pulse is taken into consideration. Hence, we propose that trap filling is the dominant mechanism that is responsible for the dependences of the PL time profiles on the excitation intensity and pulse frequency.

It should be noted again that the photogenerated charge carriers might diffuse into the bulk over a few micrometers prior to interfacial charge transfer during the slow charge-transfer process. To reveal whether or not the charge carriers in $MAPbBr_3$ survive prior to charge trapping or charge transfer to the $MAPbBr_{3-x}I_x$ phase, we performed time-resolved THz experiments. THz signals are proportional to the concentration of charges and their mobility, thereby providing information on the time evolution of mobile charges in the perovskite. $MAPbBr_3$ crystals were spin-coated onto quartz glass, followed by halide exchange for the same reaction time and with the same MAI concentration as used in the PL experiments. A 400-nm fs pulsed laser (38–52 μJ cm^{-2}) was used as the light source. Figure 3B shows decay profiles before and after reaction. The profile exhibited no decay for 100 ps before the reaction, but it exhibited a small decay component following the reaction. The profile after the reaction was fitted by a single exponential function with a lifetime of 318 ± 66 ps. This decay component is attributed to trapping and charge transfer. From the THz profiles, 72 ± 5% of the mobile charges survive for 100 ps without deactivation, potentially resulting in slow charge transfer.

Chae et al. showed that the incorporation of chloride ions into $MAPbI_3$ films occurs non-uniformly, with heterogeneity decreasing with increasing annealing time.[39] They suggested that the mixed-halide perovskite film initially consists of a mixture of Cl-rich and Cl-deficient phases. Moreover, Draguta et al. reported that trap sites are distributed inhomogeneously in perovskite thin films, as revealed by space-resolved PL decay experiments.[40] Our previous study also showed inhomogeneous halide exchange by in-situ PL imaging and revealed that the migration of halide

ions is related to halide vacancies at the surface.[14] We consider that the inhomogeneous distribution of trap sites is intrinsic to $MAPbBr_3$ crystals and affects the exchange reaction and charge-transfer process. Therefore, to further investigate the relationship between the trap-state distribution and charge-transfer kinetics, we conducted space-resolved PL experiments on a $MAPbBr_3$ crystal following the exchange reaction.

PL decay profiles and spectra of pure $MAPbBr_3$ and $MAPbBr_{3-x}I_x$ were recorded on the reacted crystal by confocal microscopy. Figure 4A displays the integrated PL-intensity image obtained for $MAPbBr_{3-x}I_x$ (step size: 200 × 200 nm). The data captured at three locations in Figure 4A clearly exhibit different profiles (Figure 4B). The variation among the profiles acquired at different locations on the $MAPbBr_{3-x}I_x$ crystal infers an inhomogeneous distribution of trap sites. To reveal the effect of trap filling on charge-transfer dynamics, the correlation between the $MAPbBr_{3-x}I_x$ PL rise time and the $MAPbBr_3$ PL mean lifetime was examined at 16 points on the same crystal, the results of which are shown in Figure 4C, which clearly demonstrates that the rise time correlates positively with decay lifetime, highlighting that trap filling also suppresses further trapping processes leading to a prolonged decay lifetime.

To reveal such a suppressed trapping process, the $MAPbBr_3$ decay profile at each point was fitted by a triexponential function with the lifetimes of τ_1, τ_2 and τ_3, and the amplitude contributions of the three decay components were examined (Figure 4D). The fraction of the fast decay component (τ_1) increased with increasing rise time (circles in Figure 4D), while the middle decay component (τ_2) decreased (squares in Figure 4D). Interestingly, the dominant decay component with the τ_1 lifetime become minor in the lower rise-time range ($\tau_{rise} < 1$ ns), although the value of τ_1 remained constant. As shown in Figure 2A, τ_1 is attributed to hole transfer to the $MAPbBr_{3-x}I_x$ phase. Considering that the reciprocal and fraction of τ_2 decreased for $\tau_{rise} > 1$ ns in Figure 4D, τ_2

is attributed to the trapping process because this trapping process is suppressed due to trap filling. In the lower rise-time range (τ_{rise} < 1 ns), on the other hand, the trap states are vacant leading to less band bending and a dominant trapping process, whereas in the higher rise-time range, the trap states on $MAPbBr_3$ are occupied by charge carriers leading to band bending and suppressed trapping. Note that the excitation power density was 0.81 μJ cm^{-2}. From these excitation-dependence experiments, we conclude that the trap states are not fully filled at all of the locations examined.

The effect of trap filling on the slow transfer process (τ_{rise} > 1 ns) is also revealed by the PL-intensity correlation. Figure 4E displays the correlation between rise time and PL intensity. Green PL from $MAPbBr_3$ was suppressed at the lower rise time due to dominant trapping, whereas the intensity increased at higher rise times due to trap filling. Interestingly, red PL from $MAPbBr_{3-x}I_x$ displayed the inverse trend to that of $MAPbBr_3$. If trap filling affects the charge transfer process, suppressed trapping would result in an increase in the PL from $MAPbBr_{3-x}I_x$ at higher rise times, although the opposite trend was observed. In our previous study, the relationship between halogen-ion migration and halide vacancies at the surface was revealed.[14] Given this relationship and our results, we suggest that the degree of trap filling correlates negatively with the concentration of the $MAPbBr_{3-x}I_x$ domains. Incorporation of iodide into $MAPbBr_3$ alters the surface composition and structure, which affects its charge-trapping nature. Actually, inhomogeneous iodide concentration was observed within an individual crystal by energy dispersive X-ray spectroscopy (EDS) coupled with scanning transmission electron microscopy (STEM) (Figure S2). Moreover, different trapped-carrier lifetimes were measured for $MAPbI_3$ films prepared by spin-coating and gas-assisted techniques.[16] The wide range of the transfer rates originates from the heterogeneous distributions of trap sites and iodide-rich domains.

Taken together, the key findings are summarized as follows:

(1) The electron-transfer rate determines the rise component in the PL profile of $MAPbBr_{3-x}I_x$ (Figure 2A).

(2) Higher excitation intensity and pulse-repetition frequency lead to a lower transfer rate (Figures 2C and 3A).

(3) The transfer rate can be quite different for different locations on the reacted crystal (Figure 4B).

(4) Slower charge transfer correlates with slower trapping (Figure 4D).

To explain these results, we propose the mechanism shown in Figure 5. When the trap sites are vacant (low trapped-carrier density in Figure 5 left), the photogenerated carriers are transferred from the bulk $MAPbBr_3$ to the trap sites and to the surface $MAPbBr_{3-x}I_x$ domains with sub-nanosecond times, as usually observed for perovskite films and in mixed-halide perovskites. The vacant trap sites provide a prompt deactivation pathway through the nonradiative recombination of charge carriers. However, once the photogenerated carriers have been captured by the trap states at the surface, the trapped carriers remain there for a few hundred nanoseconds; consequently, the trap states are filled at high excitation intensities and repetition frequencies as shown in the initial process at high trapped-carrier density shown in Figure 5. In these cases, the trap sites can be considered to be interstitial iodine ions that capture holes (the attributes of the trap sites are discussed below). The trapped holes then generate an electric field that is responsible for the downward band bending.[41] Trap filling and band bending may greatly alter the charge-carrier dynamics. In the first few nanoseconds (t < 1 ns), when the trapped-carrier density is high, the trapping pathway is limited by trap filling and the photogenerated electrons near the surface are consumed through nonradiative recombinations with trapped holes (the initial process at high

trapped-carrier density shown in Figure 5). The decreased electron density near the surface due to this nonradiative recombination leads to a slower charge-transfer rate. After this process (t > 1 ns), the downward band bending due to trapped holes allows escaped electrons to diffuse from the bulk to the surface, followed by electron transfer to the surface $MAPbBr_{3-x}I_x$ domains (the diffusion process at high trapped carrier density in Figure 5). Considering that the electron-transfer rate determines the rise component in the PL profile of $MAPbBr_{3-x}I_x$, the slow rise components in the PL profiles are attributable to both 1) the decreased electron density near the surface by nonradiative recombination within a few nanoseconds, and 2) subsequent electron migration to the surface over several nanoseconds. Although it is unclear if the band structures are already bent prior to pulse excitation, interstitial iodide ions distributed over the surface should capture holes and lead to band bending, which drives electron migration. A theoretical study has suggested that interstitial iodine atoms form deep mid-gap states with low formation energies (–0.03 eV on a flat surface and –0.12 eV on vacant surface under iodine-rich conditions).[42] Moreover, Meggiolaro et al. reported that negatively charged interstitial iodide (I_i^-) is the stable defect under medium conditions (1:1 ratio of PbI_2 to MAI), which traps holes at an energy of 0.3 eV above the VB edge.[43] The addition of the MAI solution during the exchange reaction not only creates $MAPbBr_{3-x}I_x$ domains, but also interstitial defect sites. Such trap sites are inhomogeneously distributed over the crystal surface and are filled with photogenerated holes at high excitation intensity and repetition frequency due to the slow relaxations of deeply trapped carriers. Considering that the density of trap sites that results in trap filling has been reported to be ~10^{16} cm^{-3},[37,38] and that the density of photogenerated charge pairs employed here was 6×10^{15}–5×10^{17} cm^{-3}, the filling factor of the trap states is tunable under the present conditions. The degree of band bending depends on the concentration of trapped holes; hence a higher trapped-hole density leads

to a lower electron-transfer rate. This mechanism reasonably explains observations 1–4 summarized above.

To provide evidence in support of this mechanism, we numerically simulated the charge-transfer processes using a home-built program. Since charge carriers can diffuse over the entire crystal in the observed time, the time evolution of charge density in the bulk $MAPbBr_3$ can be described by one-dimensional diffusion equations that include electric potential terms:

$$\frac{\partial n_{\mathrm{e}}(x,t)}{\partial t} = D\frac{\partial^2 n_{\mathrm{e}}(x,t)}{\partial x^2} + \mu\frac{\partial}{\partial x}\big(E(x,t)n_{\mathrm{e}}(x,t)\big) - k_{\mathrm{rad}}n_{\mathrm{e}}(x,t)n_{\mathrm{h}}(x,t) - k_{\mathrm{nr}}n_{\mathrm{e}}(x,t) - \delta(x)k_{\mathrm{et}}n_{\mathrm{e}}(x,t)\Big(I(x,t) - n_{\mathrm{I,e}}(x,t)\Big) - \delta(x)k_{\mathrm{cr}}n_{\mathrm{e}}(x,t)n_{\mathrm{t}}(x,t) \quad (1)$$

$$\frac{\partial n_{\mathrm{h}}(x,t)}{\partial t} = D\frac{\partial^2 n_{\mathrm{h}}(x,t)}{\partial x^2} - \mu\frac{\partial}{\partial x}\big(E(x,t)n_{\mathrm{h}}(x,t)\big) - k_{\mathrm{rad}}n_{\mathrm{e}}(x,t)n_{\mathrm{h}}(x,t) - k_{\mathrm{nr}}n_{\mathrm{h}}(x,t) - \delta(x)k_{\mathrm{ht}}n_{\mathrm{h}}(x,t)\Big(I(x,t) - n_{\mathrm{I,h}}(x,t)\Big) - \delta(x)k_{\mathrm{t}}n_{\mathrm{h}}(x,t)\big(N_{\mathrm{t}}(x,t) - n_{\mathrm{t}}(x,t)\big) \quad (2)$$

where $n_{\mathrm{e}}(x,t)$ and $n_{\mathrm{h}}(x,t)$ are the concentrations of electrons and holes in the bulk $MAPbBr_3$, respectively, and $n_{\mathrm{I,e}}(t)$ and $n_{\mathrm{I,h}}(t)$ are the concentrations of electrons and holes in the $MAPbBr_{3-x}I_x$ domains, respectively ($0 \le x \le L$; L is the thickness of the crystal). Since the transfer rates for the electrons and holes appear to be different, each diffusion equation needs to be considered independently. In these equations D is the diffusion coefficient of charge carriers in the bulk $MAPbBr_3$, μ is the charge-carrier mobility, and $E(x,t)$ is the electric field induced by the trapped holes. In addition, k_{rad} and $k_{\mathrm{I,rad}}$ are the rate constants for radiative recombination in $MAPbBr_3$ and $MAPbBr_{3-x}I_x$, respectively, k_{nr} and $k_{\mathrm{I,nr}}$ are the trapping rate constants as a result of the intrinsic

trap sites in $MAPbBr_3$ and $MAPbBr_{3-x}I_x$, respectively, k_{et} and k_{ht} are the rate constants for electron and hole transfer, respectively, and $I(t)$ is the concentration of the $MAPbBr_{3-x}I_x$ domains. Considering that the nanosized $MAPbBr_{3-x}I_x$ domains are present only on the surface, the transfer rates should be proportional to $(I(t) - n_{I,e(h)}(t))$. In addition, N_t and n_t are the concentrations of the hole-trap sites and trapped holes, respectively, k_t is the trapping rate constant that provides electric field $E(x,t)$, and k_{cr} is the rate constant for trapped-hole relaxation through nonradiative charge recombination with CB electrons. $(N_t(t) - n_t(t))$ assures the effect of trap filling. The time evolution of the charge-carrier density in the $MAPbBr_{3-x}I_x$ domains, $n_{I,e(h)}(t)$, and trap sites, $n_t(t)$, can be expressed by the following differential equations:

$$\frac{\partial n_{\mathrm{I,e}}(x,t)}{\partial t} = \delta(x)k_{\mathrm{et}}n_{\mathrm{e}}(x,t)\left(I(x,t) - n_{\mathrm{I,e}}(x,t)\right) - k_{\mathrm{I,rad}}n_{\mathrm{I,e}}(x,t)n_{\mathrm{I,h}}(x,t) - k_{\mathrm{I,nr}}n_{\mathrm{I,e}}(x,t) \quad (3)$$

$$\frac{\partial n_{\mathrm{I,h}}(x,t)}{\partial t} = \delta(x)k_{\mathrm{ht}}n_{\mathrm{h}}(x,t)\left(I(x,t) - n_{\mathrm{I,h}}(x,t)\right) - k_{\mathrm{I,rad}}n_{\mathrm{I,e}}(x,t)n_{\mathrm{I,h}}(x,t) - k_{\mathrm{I,nr}}n_{\mathrm{I,h}}(x,t) \quad (4)$$

$$\frac{\partial n_{\mathrm{t}}(x,t)}{\partial t} = \delta(x)k_{\mathrm{t}}n_{\mathrm{h}}(x,t)\big(N_{\mathrm{t}}(x,t) - n_{\mathrm{t}}(x,t)\big) - \delta(x)k_{\mathrm{cr}}n_{\mathrm{e}}(x,t)n_{\mathrm{t}}(x,t) \quad (5)$$

In eqs 1–5, the $MAPbBr_{3-x}I_x$ domains and hole-trap sites are assumed to be homogeneously distributed near the surface to a depth d, and $\delta(x)$ assures that charge transfer and hole trapping occur only within d:

$$N_{\mathrm{t}}(x,t) = \begin{cases} N_{\mathrm{t0}} & 0 \le x \le d \\ 0 & x > d \end{cases} \quad (6)$$

$$I(x,t) = \begin{cases} I_0 & 0 \le x \le d \\ 0 & x > d \end{cases} \quad (7)$$

$$\delta(x) = \begin{cases} 1 & 0 \le x \le d \\ 0 & x > d \end{cases} \quad (8)$$

The electric potential $V(x,t)$ satisfies the Poisson's equation:

$$\frac{\partial^2 V(x,t)}{\partial x^2} = -e\frac{n_t(x,t)}{\varepsilon\varepsilon_0} \quad (9)$$

where e is the unit charge, ε is the effective dielectric constant, and ε_0 is the vacuum permittivity. From eqs 6–9, the electric field $E(x,t)$ and electric potential $V(x,t)$ are expressed as:

$$V(x,t) = -\frac{en_t(x,t)}{2\varepsilon\varepsilon_0}(x-d)^2 \quad (10)$$

$$E(x,t) = -\frac{en_t(x,t)}{\varepsilon\varepsilon_0}(x-d) \quad (11)$$

The trapped-hole concentration, $n_t(t)$, varies over time due to trapping and nonradiative recombination with CB electrons; therefore the electric field is also time-dependent and affects the carrier distribution dynamically. By solving the above equations, the densities of the carriers in the $MAPbBr_3$ and $MAPbBr_{3-x}I_x$ phases and the trap sites on the crystal surface can be simulated at a delay time t.

To simulate the dependences of the PL profiles on the photogenerated carrier density, the densities and rate constants were set as free parameters, and the same values were used to analyze each set of data. The initial carrier density was calculated using the sample thickness L, excitation power density, and absorption coefficient α at 405 nm (= 8.5×10^4 cm^{-1}) of $MAPbBr_3$.[19] The PL

profiles of $MAPbBr_3$ and $MAPbBr_{3-x}I_x$ were obtained by calculating $k_{rad} \cdot n_e(x,t) \cdot n_h(x,t)$ and $k_{I,rad} \cdot n_{I,e}(x,t) \cdot n_{I,h}(x,t)$, respectively. Note that since PL was detected in our experiments from depths of only a few hundred nanometers (~300 nm), radiative recombination at depths over 300 nm was excluded from the calculation.

Figure 6A shows the simulated PL decay profiles for the $MAPbBr_{3-x}I_x$ phase, which qualitatively reproduces the observed dependence on excitation power density. The fitting parameters in this study are presented in Table 1, in which some parameters were set by referring to reported values. The higher density of photogenerated charge pairs leads to a slower rise time for the $MAPbBr_{3-x}I_x$ phase, as observed in Figure 2C. No rise components were observed in the simulated profiles in the absence of the electric potential (Figure S3). We also simulated the dependence on trapped carrier density by setting all parameters to the same conditions, with the exception of the initial concentration of trapped holes. Figure 6B clearly shows that the rise time increases with increasing initial concentration of trapped holes.

To validate our simulation, the excitation-density dependence of the PL intensity was simulated. Figure 6C displays the relationship between PL intensity and excitation-power density on a double-logarithmic scale. From the linear fit, the slope for $MAPbBr_3$ was determined to be ~2, which indicates that bimolecular recombination increases with increasing excitation intensity due to trap filling. This slope for $MAPbBr_{3-x}I_x$ was less than unity, which is attributable to photogenerated carriers lost in the bulk $MAPbBr_3$ by radiative recombination and trapping prior to charge transfer. Furthermore, taking into consideration that the hole-transfer rate is faster than the electron-transfer rate, radiative recombination can be described by pseudo-first-order kinetics with respect to hole concentration. However, the slope for $MAPbBr_{3-x}I_x$ increased at higher excitation intensities, indicating that the carrier loss by trapping was suppressed due to trap filling. The simulation also

showed a similar trend. Therefore, the simulation results are consistent with our proposed mechanism and verify our simulation model.

The macroscopic properties of mixed-halide perovskites are mainly determined by their halide compositions, whereas the carrier dynamics at the surface or interfaces with conductive substrates or charge-transport layers are significantly modulated by locally distorted band structures. From our findings, we suggest that excess halide ions are introduced as hole traps during exchange reactions, leading to a photoinduced change in band bending. This situation is more pronounced when concentrated light is irradiated into a photovoltaic cell. Furthermore, the removal of such traps by a suitable post-treatment following halide substitution might avoid deterioration of device performance.

CONCLUSION

In conclusion, slow charge-transfer over a few nanoseconds was observed for perovskites partially substituted with iodide. Using space- and time-resolved PL microscopy, we elucidated the details of the charge-transfer process from the bulk $MAPbBr_3$ to the surface $MAPbBr_{3-x}I_x$ domains on the nanometer scale. Charge-transfer rates across the interface between two different structures were found to correlate with trapping rates in the $MAPbBr_3$; slower trapping rates led to higher PL intensities from $MAPbBr_3$, while slower charge-transfer rates indicate that trap filling is mainly responsible for the slow transfer process. It appears that the addition of the MAI solution during the halide exchange reaction not only results in the formation of $MAPbBr_{3-x}I_x$ domains, but also trap sites on the crystal surface. Interstitial I^- ions are most likely introduced as deep hole traps, and the filling of these trap states with holes induces potential variations in the space charge

region. To support our proposed mechanism, we numerically simulated the effect of electric field using the diffusion model, the results of which explain our observations very well. Our findings suggest that trapped charges modulate the charge-transfer processes in nanometer-scale heterostructured perovskites. By taking into account the electric fields caused by trapped charges, band tuning through partial halide substitution will become a sophisticated approach for the fabrication of highly efficient devices.

METHODS

Chemicals. Lead(II) bromide ($PbBr_2$, 99%, Sigma-Aldrich), methylamine (33 wt% in absolute ethanol, Sigma-Aldrich), hydrobromic acid (48 wt% in water, Tokyo Chemical Industry), methylammonium iodide (98%, Tokyo Chemical industry), 2-propanol (super dehydrated, >99.7%, Wako Pure Chemical Industries), *N*,*N*-dimethylformamide (DMF, super dehydrated, >99.5%, Wako Pure Chemical Industries), and diethyl ether (super dehydrated, >99.5%, Wako Pure Chemical Industries) were used as received without further purification. Methylammonium bromide (MABr) was synthesized by the reaction of methylamine with hydrobromic acid. Hydrobromic acid first was added to the above-mentioned methylamine solution with stirring at 0 °C for 2 h. A solid was obtained upon evaporating the solvent at 45 °C, which was washed three times with diethyl ether and dried under vacuum for further use.

Sample Preparation and Characterization. Microsized $MAPbBr_3$ crystals were synthesized following the procedure in our previous report.[14] The slow addition of toluene into a precursor solution containing equimolar amounts of MABr and $PbBr_2$ in DMF, produced orange-colored $MAPbBr_3$ crystals. The resultant crystals were purified by washing several times with toluene. The

$MAPbBr_3$ crystals were deposited on a glass coverslip by spin-coating a suspension of the crystals. The solution for the halide-exchange reaction was prepared by mixing a 2-propanol solution of MAI with heptane, followed by filtration to remove the insoluble salt. The concentration of MAI in the solution was determined to be 0.22 mM by NMR spectroscopy. A 2-μL aliquot of the reaction solution was then added to a sample chamber filled with 2 mL of heptane to initiate the exchange reaction. Transmission electron microscopy (TEM) was performed using a JEM-2100F (JEOL) microscope, with an accelerator voltage of 200 kV.

PL Spectromicroscopy Measurements. The experimental spectromicroscopy setup was based on a Nikon Ti-E inverted fluorescence microscope. A 405-nm pulsed-diode laser (PiL040X, Advanced Laser Diode System), with a pulse width of ~45 ps (FWHM) was used to excite the sample through an objective lens (CFI Plan Apo λ 100×H, Nikon; NA 1.45). Time-resolved PL experiments were performed using a home-built confocal microscope system. Emitted photons were passed through a 100-μm pinhole and a longpass filter (ET425lp, Chroma), and then directed onto a single-photon avalanche diode (SPAD; SPD-050, Micro Photon Devices). The signals from the SPAD were sent to a time-correlated single photon counting (TCSPC) module (SP-130EM, Becker & Hickl) for further analysis. The data were analyzed using the Origin 2018 software (OriginLab). All experimental data were acquired at room temperature.

Time-Resolved THz Measurements. A Ti:sapphire regenerative amplifier was used to generate a 100 fs pulse with a 1 kHz repetition rate, centered at a wavelength of 800 nm. The output was split into three, and was used for optical excitation of the sample, terahertz (THz) wave generation, and detection. A 400-nm pump pulse was generated in a 1-mm-thick β-BaB_2O_4 (BBO) crystal. THz probe pulses were generated by femtosecond laser-induced plasma. Other 0.1-mm-thick BBO crystals were used to generate a second harmonic pulse. Both the fundamental and second

harmonic pulses were focused into nitrogen gas to produce a THz pulse by ionizing the gas at the focal position. The THz pulse was collimated and focused onto the sample with a pair of gold-coated parabolic mirrors, and overlapped collinearly with the optical pump pulses. The electric fields of the THz probe pulses were measured beyond the sample using an air-biased coherent detection scheme; this was achieved by mixing THz pulses with the third 800-nm detection pulse in order to measure the generation of the THz-induced second harmonic. A high-voltage AC bias field of 1.5 kV was applied at the focal position to produce a local oscillator for heterodyne detection.

Numerical Simulation. Derivatives with respect to time and space were used to numerically solve the one-dimensional diffusion relationships described by eqs 1 and 2. The partial differential equation (eqs 3–5) were solved numerically using derivatives with respect to time. The sample thickness L was determined on the basis of the optical transmission image. Numerical calculations were performed using MATLAB (The MathWorks).

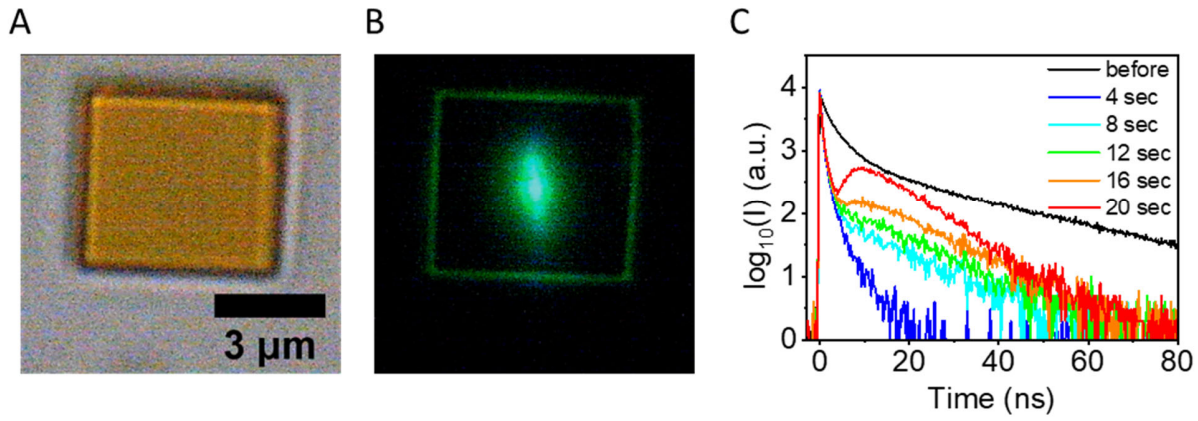

Figure 1. (A) Optical and (B) PL images of the $MAPbBr_3$ crystal before reaction. Wide-field images were captured with a color CCD camera. The green PL emission in the center of panel B corresponds to the excitation-laser spot. (C) PL decay profiles at different reaction times *T* at an excitation power density of 0.81 μJ cm^{-2}.

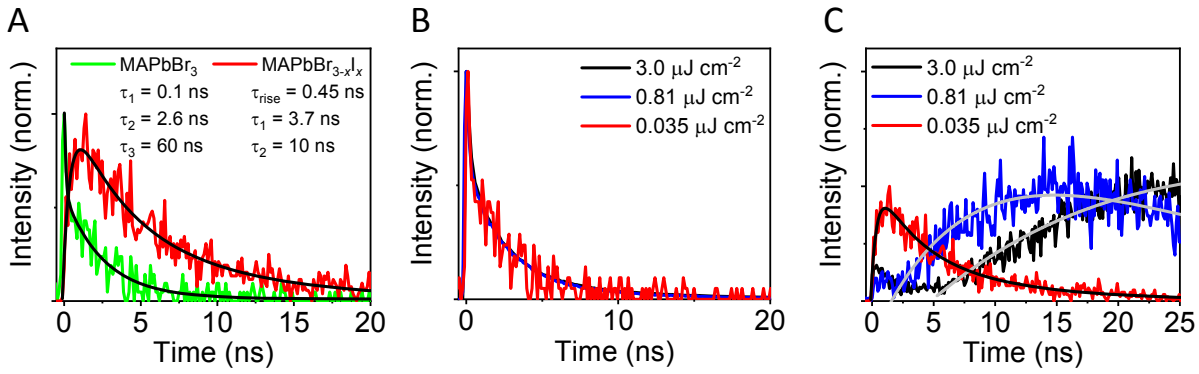

Figure 2. (A) PL decay profiles of $MAPbBr_3$ (green solid trace) and $MAPbBr_{3-x}I_x$ (red solid trace); 515–560 nm and 630–800 nm bandpass filters were used for $MAPbBr_3$ and $MAPbBr_{3-x}I_x$, respectively. The profiles were well fitted by triexponential functions (black solid lines). The PL decay profiles of (B) $MAPbBr_3$ and (C) $MAPbBr_{3-x}I_x$ at various excitation power densities. The profiles at both 0.81 μJ cm^{-2} and 0.035 μJ cm^{-2} were fitted to biexponential curves (gray solid lines). The black solid line is the same triexponential curve as shown in panel A.

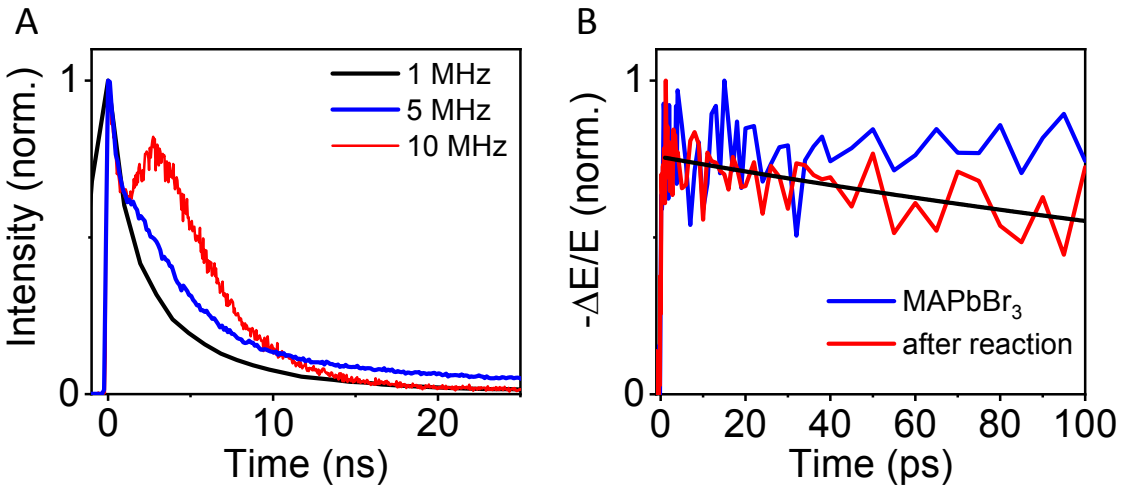

Figure 3. (A) PL decay profiles of $MAPbBr_{3-x}I_x$ (630–800 nm bandpass filters were used) at various pulse-repetition frequencies at an excitation-power density of 0.81 μJ cm^{-2}. (B) THz decay profiles of $MAPbBr_3$ before (blue solid trace) and after the exchange reaction (red solid trace). The decay profile of the treated sample was fitted by a single exponential function (black solid line). The excitation power densities were 38 μJ cm^{-2} for $MAPbBr_3$ and 52 μJ cm^{-2} for $MAPbBr_{3-x}I_x$.

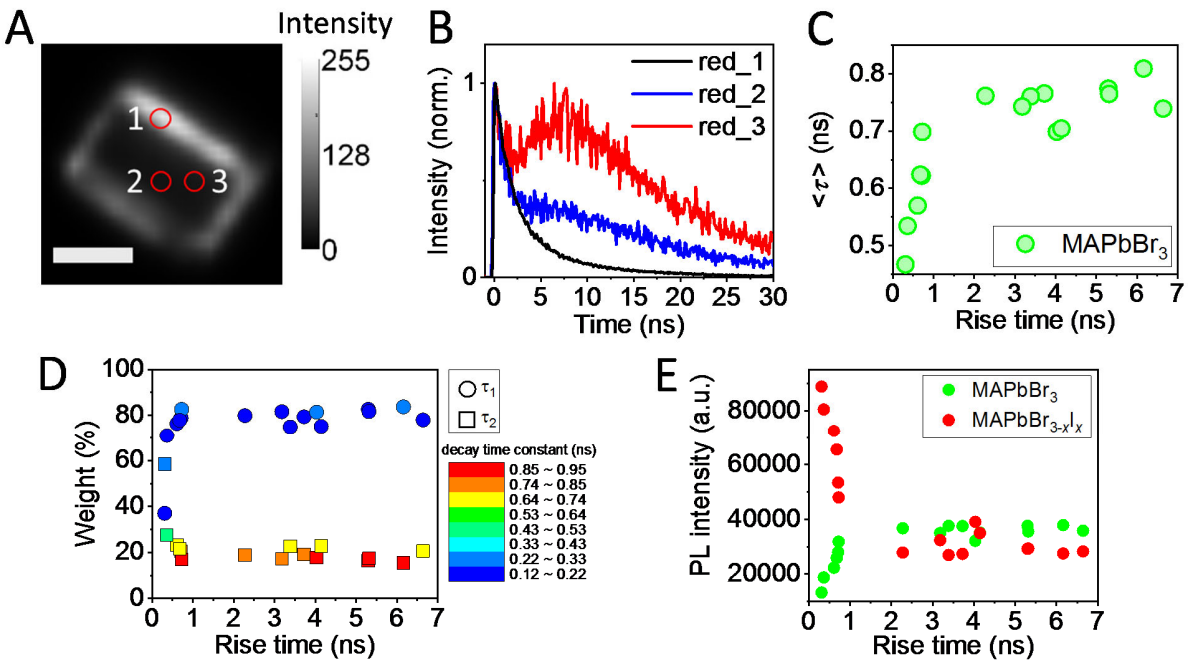

Figure 4. (A) PL intensity image of an $MAPbBr_{3-x}I_x$ crystal (630–800 nm bandpass filters were used) after the exchange reaction. Step size: 200 × 200 nm; scale bar: 2 μm. (B) PL decay profiles acquired from the indicated positions in panel A. (C) Correlation between the $MAPbBr_{3-x}I_x$ rise time and $MAPbBr_3$ mean lifetime ($<\tau>$) for 16 points on the crystal shown in panel A. (D) Correlations between rise times and weights of the fast (τ_1) and middle (τ_2) decay components. The time-constant values are indicated by the color scale. (E) Correlations between the rise times and PL intensities for $MAPbBr_3$ (green) and $MAPbBr_{3-x}I_x$ (red).

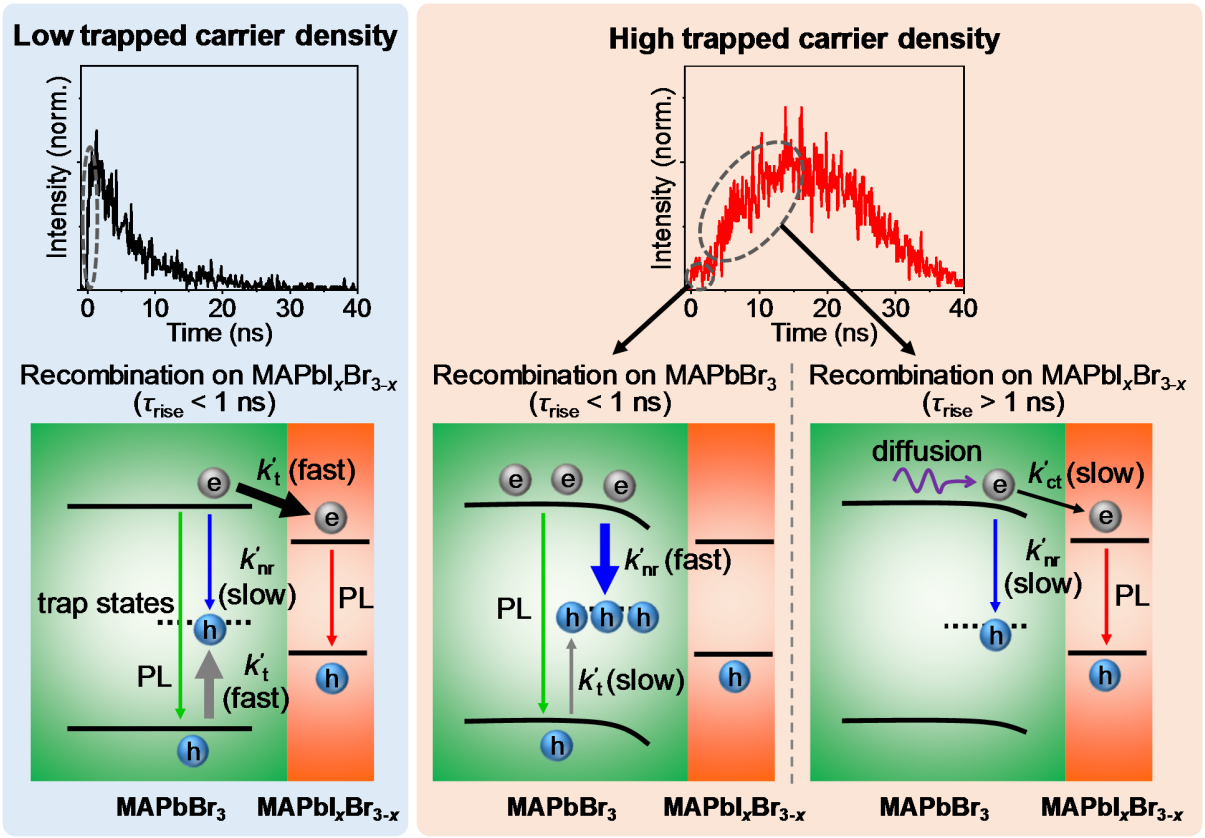

Figure 5. Schematic illustration of the proposed mechanism. The letters "h" and "e" represent hole and electron, respectively, while k'_{ct} (black arrows), k'_{nr} (blue arrows), and k'_t (gray arrows) represent the rates of electron transfer, nonradiative recombination, and trapping, respectively. Thicker arrows indicate faster rates.

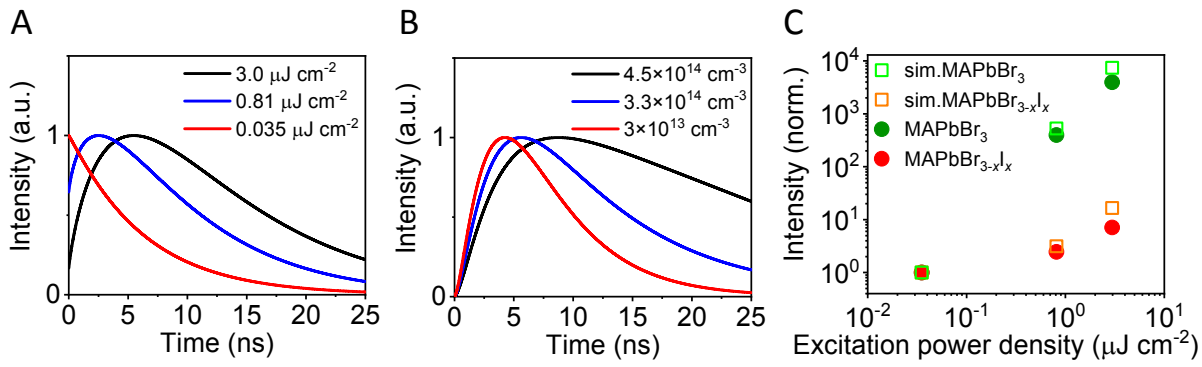

Figure 6. (A) Simulated PL profiles for $MAPbBr_{3-x}I_x$ as functions of excitation power. Only the initial carrier density $n_{e(h)}$ (t = 0) was varied. (B) Simulated PL profiles for $MAPbBr_{3-x}I_x$ as functions of trapped-carrier density. Only the initial trapped-hole concentration n_t (t = 0) was varied. (C) Excitation power dependence of the PL intensity. Circles and squares represent experimental and the simulated values, respectively.

Table 1. Parameters Used to Simulate the PL Decay Profiles

Parameters	Excitation power dependence	Trapped hole dependence
L [m]	5×10^{-6}	5×10^{-6}
D [$cm^2\ s^{-1}$]	0.3 [26]	0.1 [26]
μ [$cm^2\ V^{-1}\ s^{-1}$]	100 [44]	80 [44]
ε	28 [45]	28
N_t [cm^{-3}]	1×10^{16}	3×10^{16}
I [cm^{-3}]	1×10^{17}	1×10^{18}
d [m]	10×10^{-9}	10×10^{-9}
k_t [$cm^3\ s^{-1}$]	1×10^{-10} [37]	1×10^{-10}
k_{cr} [$cm^3\ s^{-1}$]	1×10^{-11} [37]	1×10^{-11}
k_{rad} [$cm^3\ s^{-1}$]	4×10^{-10} [26]	4×10^{-10}
k_{nr} [s^{-1}]	8×10^{7}	8×10^{7}
$k_{I,rad}$ [$cm^3\ s^{-1}$]	8×10^{-11}	8×10^{-11}
$k_{I,nr}$ [s^{-1}]	8×10^{7}	2×10^{8}
k_{et} [$cm^3\ s^{-1}$]	1×10^{-10}	3×10^{-10}
k_{ht} [$cm^3\ s^{-1}$]	5×10^{-10}	9×10^{-10}

ASSOCIATED CONTENT

Supporting Information. The Supporting Information is available free of charge on the ACS Publications website.

PL spectrum, STEM image, and simulation results (PDF)

AUTHOR INFORMATION

Corresponding Author

*E-mail: tachikawa@port.kobe-u.ac.jp; TEL: +81-78-803-5736.

Notes

The authors declare no competing financial interest.

ACKNOWLEDGMENT

We thank Prof. Keisuke Tominaga (Molecular Photoscience Research Center, Kobe University) for fruitful discussion. This work was partially supported by JSPS KAKENHI Grant Numbers JP15H03771, JP18H01944, JP18H04517, and others.

REFERENCES

(1) Green, M. A.; Ho-Baillie, A.; Snaith, H. J. The Emergence of Perovskite Solar Cells. *Nat. Photonics* **2014**, *8*, 506–514.

(2) Yamada, Y.; Nakamura, T.; Endo, M.; Wakamiya, A.; Kanemitsu, Y. Photocarrier Recombination Dynamics in Perovskite $CH_3NH_3PbI_3$ for Solar Cell Applications. *J. Am. Chem. Soc.* **2014**, *136*, 11610–11613.

(3) Ponseca, C.; Savenije, T.; Abdellah, M.; Zheng, K.; Yartsev, A.; Pascher, T.; Harlang, T.; Chabera, P.; Pullerits, T.; Stepanov, A.; Wolf, J.; Sundström, V. Organometal Halide Perovskite Solar Cell Materials Rationalized: Ultrafast Charge Generation, High and Microsecond-Long Balanced Mobilities, and Slow Recombination. *J. Am. Chem. Soc.* **2014**, *136*, 5189–5192.

(4) National Center for Photovoltaics at the National Renewable Energy Laboratory. https://www.nrel.gov/pv/assets/images/efficiency-chart.png.

(5) Zhu, H.; Fu, Y.; Meng, F.; Wu, X.; Gong, Z.; Ding, Q.; Gustafsson, M. V.; Trinh, M. T.; Jin, S.; Zhu, X. Y. Lead Halide Perovskite Nanowire Lasers with Low Lasing Thresholds and High Quality Factors. *Nat. Mater.* **2015**, *14*, 636–642.

(6) Tan, Z.-K.; Moghaddam, R. S.; Lai, M. L.; Docampo, P.; Higler, R.; Deschler, F.; Price, M.; Sadhanala, A.; Pazos, L. M.; Credgington, D.; Hanusch, F.; Bein, T.; Snaith, H. J.; Friend, R. H. Bright Light-Emitting Diodes Based on Organometal Halide Perovskite. *Nat. Nanotechnol.* **2014**, *9*, 687–692.

(7) Tachikawa, T.; Karimata, I.; Kobori, Y. Surface Charge Trapping in Organolead Halide Perovskites Explored by Single-Particle Photoluminescence Imaging. *J. Phys. Chem. Lett.* **2015**, *6*, 3195–3201.

(8) de Quilettes, D. W.; Vorpahl, S. M.; Stranks, S. D.; Nagaoka, H.; Eperon, G. E.; Ziffer, M. E.; Snaith, H. J.; Ginger, D. S. Impact of Microstructure on Local Carrier Lifetime in Perovskite Solar Cells. *Science* **2015**, *348*, 683 LP-686.

(9) Jeon, N. J.; Noh, J. H.; Yang, W. S.; Kim, Y. C.; Ryu, S.; Seo, J.; Seok, S. Il. Compositional Engineering of Perovskite Materials for High-Performance Solar Cells. *Nature* **2015**, *517*, 476–480.

(10) Noh, J. H.; Im, S. H.; Heo, J. H.; Mandal, T. N.; Seok, S. Il. Chemical Management for Colorful, Efficient, and Stable Inorganic-Organic Hybrid Nanostructured Solar Cells. *Nano Lett.* **2013**, *13*, 1764–1769.

(11) Jang, D. M.; Park, K.; Kim, D. H.; Park, J.; Shojaei, F.; Kang, H. S.; Ahn, J. P.; Lee, J. W.; Song, J. K. Reversible Halide Exchange Reaction of Organometal Trihalide Perovskite Colloidal Nanocrystals for Full-Range Band Gap Tuning. *Nano Lett.* **2015**, *15*, 5191–5199.

(12) Kim, M. C.; Kim, B. J.; Son, D. Y.; Park, N. G.; Jung, H. S.; Choi, M. Observation of Enhanced Hole Extraction in Br Concentration Gradient Perovskite Materials. *Nano Lett.* **2016**, *16*, 5756–5763.

(13) Tian, W.; Leng, J.; Zhao, C.; Jin, S. Long-Distance Charge Carrier Funneling in Perovskite Nanowires Enabled by Built-in Halide Gradient. *J. Am. Chem. Soc.* **2017**, *139*, 579–582.

(14) Karimata, I.; Kobori, Y.; Tachikawa, T. Direct Observation of Charge Collection at Nanometer-Scale Iodide-Rich Perovskites during Halide Exchange Reaction on $CH_3NH_3PbBr_3$. *J. Phys. Chem. Lett.* **2017**, *8*, 1724–1728.

(15) Liao, Q.; Hu, K.; Zhang, H.; Wang, X.; Yao, J.; Fu, H. Perovskite Microdisk Microlasers Self-Assembled from Solution. *Adv. Mater.* **2015**, *27*, 3405–3410.

(16) Wen, X.; Feng, Y.; Huang, S.; Huang, F.; Cheng, Y.-B.; Green, M.; Ho-Baillie, A. Defect Trapping States and Charge Carrier Recombination in Organic-Inorganic Halide Perovskites. *J. Mater. Chem. C* **2016**, *4*, 793–800.

(17) Schulz, P.; Edri, E.; Kirmayer, S.; Hodes, G.; Cahen, D.; Kahn, A. Interface Energetics in Organo-Metal Halide Perovskite-Based Photovoltaic Cells. *Energy Environ. Sci.* **2014**, *7*, 1377–1381.

(18) Boschloo, G.; Hagfeldt, A. Characteristics of the Iodide/Triiodide Redox Mediator in Dye-Sensitized Solar Cells. *Acc. Chem. Res.* **2009**, *42*, 1819–1826.

(19) Chen, S.; Wen, X.; Sheng, R.; Huang, S.; Deng, X.; Green, M. A.; Ho-Baillie, A. Mobile Ion Induced Slow Carrier Dynamics in Organic–Inorganic Perovskite $CH_3NH_3PbBr_3$. *ACS Appl. Mater. Interfaces* **2016**, *8*, 5351–5357.

(20) Xing, G.; Mathews, N.; Sun, S.; Lim, S. S.; Lam, Y. M.; Grätzel, M.; Mhaisalkar, S.; Sum, T. C. Long-Range Balanced Electron- and Hole-Transport Lengths in Organic-Inorganic $CH_3NH_3PbI_3$. *Science* **2013**, *342*, 344 LP-347.

(21) Zhu, Z.; Ma, J.; Wang, Z.; Mu, C.; Fan, Z.; Du, L.; Bai, Y.; Fan, L.; Yan, H.; Phillips, D. L.; Yang, S. Efficiency Enhancement of Perovskite Solar Cells through Fast Electron Extraction: The Role of Graphene Quantum Dots. *J. Am. Chem. Soc.* **2014**, *136*, 3760–3763.

(22) Hoffman, J. B.; Schleper, A. L.; Kamat, P. V. Transformation of Sintered $CsPbBr_3$ Nanocrystals to Cubic $CsPbI_3$ and Gradient $CsPbBr_xI_{3-x}$ through Halide Exchange. *J. Am. Chem. Soc.* **2016**, *138*, 8603–8611.

(23) Yoon, S. J.; Draguta, S.; Manser, J. S.; Sharia, O.; Schneider, W. F.; Kuno, M.; Kamat, P. V. Tracking Iodide and Bromide Ion Segregation in Mixed Halide Lead Perovskites during Photoirradiation. *ACS Energy Lett.* **2016**, *1*, 290–296.

(24) Hoke, E. T.; Slotcavage, D. J.; Dohner, E. R.; Bowring, A. R.; Karunadasa, H. I.; McGehee, M. D. Reversible Photo-Induced Trap Formation in Mixed-Halide Hybrid Perovskites for Photovoltaics. *Chem. Sci.* **2015**, *6*, 613–617.

(25) Foley, B. J.; Marlowe, D. L.; Sun, K.; Saidi, W. A.; Scudiero, L.; Gupta, M. C.; Choi, J. J. Temperature Dependent Energy Levels of Methylammonium Lead Iodide Perovskite. *Appl. Phys. Lett.* **2015**, *106*, 243904.

(26) Tian, W.; Zhao, C.; Leng, J.; Cui, R.; Jin, S. Visualizing Carrier Diffusion in Individual Single-Crystal Organolead Halide Perovskite Nanowires and Nanoplates. *J. Am. Chem. Soc.* **2015**, *137*, 12458–12461.

(27) Pazos-Outón, L. M.; Szumilo, M.; Lamboll, R.; Richter, J. M.; Crespo-Quesada, M.; Abdi-Jalebi, M.; Beeson, H. J.; Vrućinić, M.; Alsari, M.; Snaith, H. J.; Ehrler, Bruno.; Friend, R. H.; Deschler, F. Photon Recycling in Lead Iodide Perovskite Solar Cells. *Science* **2016**, *351*, 1430 LP-1433.

(28) Diab, H.; Arnold, C.; Lédée, F.; Trippé-Allard, G.; Delport, G.; Vilar, C.; Bretenaker, F.; Barjon, J.; Lauret, J.-S.; Deleporte, E.; Garrot, D. Impact of Reabsorption on the Emission Spectra and Recombination Dynamics of Hybrid Perovskite Single Crystals. *J. Phys. Chem. Lett.* **2017**, *8*, 2977–2983.

(29) Hu, J.; Gottesman, R.; Gouda, L.; Kama, A.; Priel, M.; Tirosh, S.; Bisquert, J.; Zaban, A. Photovoltage Behavior in Perovskite Solar Cells under Light-Soaking Showing Photoinduced Interfacial Changes. *ACS Energy Lett.* **2017**, *2*, 950–956.

(30) Wu, Y.; Shen, H.; Walter, D.; Jacobs, D.; Duong, T.; Peng, J.; Jiang, L.; Cheng, Y.-B.; Weber, K. On the Origin of Hysteresis in Perovskite Solar Cells. *Adv. Funct. Mater.* **2016**, *26*, 6807–6813.

(31) Bergmann, V. W.; Guo, Y.; Tanaka, H.; Hermes, I. M.; Li, D.; Klasen, A.; Bretschneider, S. A.; Nakamura, E.; Berger, R.; Weber, S. A. L. Local Time-Dependent Charging in a Perovskite Solar Cell. *ACS Appl. Mater. Interfaces* **2016**, *8*, 19402–19409.

(32) Wojciechowski, K.; Stranks, S. D.; Abate, A.; Sadoughi, G.; Sadhanala, A.; Kopidakis, N.; Rumbles, G.; Li, C. Z.; Friend, R. H.; Jen, A. K. Y.; Snaith, H. J. Heterojunction Modification for Highly Efficient Organic-Inorganic Perovskite Solar Cells. *ACS Nano* **2014**, *8*, 12701–12709.

(33) Wu, B.; Fu, K.; Yantara, N.; Xing, G.; Sun, S.; Sum, T. C.; Mathews, N. Charge Accumulation and Hysteresis in Perovskite-Based Solar Cells: An Electro-Optical Analysis. *Adv. Energy Mater.* **2015**, *5*, 1500829.

(34) Zou, Y.; Holmes, R. J. Temperature-Dependent Bias Poling and Hysteresis in Planar Organo-Metal Halide Perovskite Photovoltaic Cells. *Adv. Energy Mater.* **2016**, *6*, 1501994.

(35) Nie, W.; Blancon, J. C.; Neukirch, A. J.; Appavoo, K.; Tsai, H.; Chhowalla, M.; Alam, M. A.; Sfeir, M. Y.; Katan, C.; Even, J.; Tretiak, S.; Crochet. J. J.; Gupta, G.; Mohite, A. D. Light-Activated Photocurrent Degradation and Self-Healing in Perovskite Solar Cells. *Nat. Commun.* **2016**, *7*, 1–9.

(36) Chen, B.; Yang, M.; Zheng, X.; Wu, C.; Li, W.; Yan, Y.; Bisquert, J.; Garcia-Belmonte, G.; Zhu, K.; Priya, S. Impact of Capacitive Effect and Ion Migration on the Hysteretic Behavior of Perovskite Solar Cells. *J. Phys. Chem. Lett.* **2015**, *6*, 4693–4700.

(37) Stranks, S. D.; Burlakov, V. M.; Leijtens, T.; Ball, J. M.; Goriely, A.; Snaith, H. J. Recombination Kinetics in Organic-Inorganic Perovskites: Excitons, Free Charge, and Subgap States. *Phys. Rev. Appl.* **2014**, *2*, 034007.

(38) Zheng, K.; Žídek, K.; Abdellah, M.; Messing, M. E.; Al-Marri, M. J.; Pullerits, T. Trap States and Their Dynamics in Organometal Halide Perovskite Nanoparticles and Bulk Crystals. *J. Phys. Chem. C* **2016**, *120*, 3077–3084.

(39) Chae, J.; Dong, Q.; Huang, J.; Centrone, A. Chloride Incorporation Process in $CH_3NH_3PbI_{3-x}Cl_x$ Perovskites via Nanoscale Bandgap Maps. *Nano Lett.* **2015**, *15*, 8114–8121.

(40) Draguta, S.; Thakur, S.; Morozov, Y. V.; Wang, Y.; Manser, J. S.; Kamat, P. V.; Kuno, M. Spatially Non-Uniform Trap State Densities in Solution-Processed Hybrid Perovskite Thin Films. *J. Phys. Chem. Lett.* **2016**, *7*, 715–721.

(41) Zhang, Z.; Yates, J. T. Band Bending in Semiconductors: Chemical and Physical Consequences at Surfaces and Interfaces. *Chem. Rev.* **2012**, *112*, 5520–5551.

(42) Uratani, H.; Yamashita, K. Charge Carrier Trapping at Surface Defects of Perovskite Solar Cell Absorbers: A First-Principles Study. *J. Phys. Chem. Lett.* **2017**, *8*, 742–746.

(43) Meggiolaro, D.; Mosconi, E.; De Angelis, F. Modeling the Interaction of Molecular Iodine with $MAPbI_3$: A Probe of Lead-Halide Perovskites Defect Chemistry. *ACS Energy Lett.* **2018**, *3*, 447–451.

(44) Semonin, O. E.; Elbaz, G. A.; Straus, D. B.; Hull, T. D.; Paley, D. W.; van der Zande, A. M.; Hone, J. C.; Kymissis, I.; Kagan, C. R.; Roy, X.; Owen, J. S. Limits of Carrier Diffusion in n−Type and p−Type $CH_3NH_3PbI_3$ Perovskite Single Crystals. *J. Phys. Chem. Lett.* **2016**, *7*, 3510–3518.

(45) Onoda-Yamamuro, N.; Matsuo, T.; Suga, H. Dielectric Study of $CH_3NH_3PbX_3$ (X = Cl, Br, I). *J. Phys. Chem. Solids* **1992**, *53*, 935–939.

TOC graphic.